(Received 13 October 2024, Accepted 26 November 2024, Scheduled 11 December 2024)

A Novel Proof-of-Concept AI-Driven Approach for Advanced Electromagnetic Imaging

Ali Ghaffarpour, Tahereh Vasei, Mahindra Ganesh, Reza K. Amineh*, and Maryam Ravan

Department of Electrical and Computer Engineering, New York Institute of Technology, New York, NY 10023, USA

ABSTRACT: This paper introduces an artificial intelligence (AI) methodology designed to enhance the output of two-dimensional (2D) electromagnetic imaging systems, specifically tailored for the imaging of conductive objects utilizing inductive sensors. The core of our imaging system comprises a commercial data acquisition board, alongside custom-made multilayer planar coils developed by conventional printed circuit board technology. By leveraging recent advances in AI and machine learning, our approach significantly improves the resolution and clarity of electromagnetic images. The paper uses a multi-layer perceptron (MLP) classifier to process the raw electromagnetic data captured by the imaging system. These algorithms are trained to recognize patterns and anomalies in electromagnetic field data, which are often indicative of conductive objects. The enhanced imaging capability is demonstrated through a series of experiments that compare the AI-enhanced outputs with the ground truth.

1. INTRODUCTION

Electromagnetic imaging of metallic objects plays a pivotal role across a diverse range of fields, encompassing infrastructure assessment, nondestructive testing, security screening, and biomedical imaging (e.g., see [1]). Within this domain, electromagnetic induction imaging (EII) emerges as a distinguished technique. It utilizes electromagnetic waves with sufficiently low frequency that can penetrate materials, thereby inducing eddy currents on the surfaces of the hidden conductive objects. These induced currents, in turn, generate secondary electromagnetic fields that propagate back to the transmitter, effectively encoding intricate details about the objects' characteristics [1, 2]. EII has found successful applications across various areas, including biomedical imaging, nondestructive testing, and national security (e.g., see [3]).

The application of EII in visualizing biological tissues has been noteworthy, with systems incorporating a planar array of coils facilitating subsurface imaging [3, 4]. Recent innovations have introduced high-sensitivity detection methods alongside resonant LCR circuits, significantly enhancing the imaging of conductive samples that are shielded by barriers [5].

Advanced EII systems have integrated techniques such as planar arrays and hemispherical arrangements to augment sensitivity and resolution [6]. Systems designed specifically for brain imaging and the detection of cerebral hemorrhages have employed hemispherical coil arrays to achieve superior sensitivity distribution [7].

It is worth noting that in recent years, deep learning techniques have gained significant attention in addressing electromagnetic inverse scattering problems, offering promising results in complex imaging scenarios. Several works have demonstrated the effectiveness of neural networks for solving such inverse problems, including microwave imaging and ground-penetrating radar applications. For instance, Franceschini et al. [8] and Ambrosanio et al. [9] have explored the use of neural networks and convolutional neural networks in microwave imaging and tomographic MIMO radar imaging, respectively. Additionally, Wei and Chen [10] and Li et al. [11] have applied deep learning schemes to full-wave nonlinear inverse scattering and nonlinear electromagnetic inverse scattering, achieving enhanced performance in these challenging tasks. These advancements underscore the potential of AI-based approaches in electromagnetic imaging which is aligned with the objectives of our proposed method here.

Figure 1 illustrates the fundamental structure of EII for imaging conductive objects. The process begins with a data acquisition system that emits electromagnetic waves from an inductor toward the conductive object. These waves interact with the object's surface, creating unique patterns captured by sensors. The data are processed by a data acquisition board, translating the electromagnetic patterns into digital signals. A computer then analyzes these signals, allowing for precise identification of the object's shape, size, and material composition.

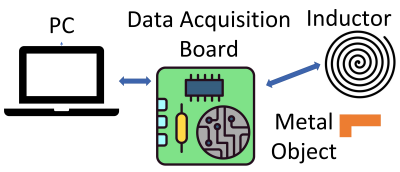

FIGURE 1. Structure of the EII for metal object detection.

To proceed toward real-time EII systems, the data acquisition process and imaging algorithms need to be expedited compared to the previous works. To implement faster data acquisition, here we propose the use of an array of coils that can be scanned

* Corresponding author: Reza K. Amineh (rkhalaja@nyit.edu).

electronically as opposed to the mechanical scanning of a single coil over the scanned aperture (e.g., see [12]). To perform faster image reconstruction, we propose to use artificial intelligence (AI) as a means to avoid using complicated and slower image reconstruction algorithms (e.g., see [12]). In particular, the integration of AI into this framework significantly amplifies the capabilities of traditional EII. AI algorithms possess the capability to rapidly process the data generated during the scanning process, identifying subtle anomalies and intricate details that might otherwise be overlooked by conventional methods.

2. DETECTION OF OBJECTS OVER A TWO-DIMENSIONAL (2D) PLANE

In the EII system, a transmitter coil emits electromagnetic waves to illuminate conductive objects. The system detects changes in the electromagnetic field caused by these objects. The transmitter coil, along with one or more receiver coils, moves in unison to scan the back-scattered electromagnetic field across the aperture. This scanning process is essential for capturing detailed data about the object's characteristics.

To enhance the sensitivity of the system in detecting secondary fields — those fields re-emitted by the conductive objects — a capacitor is connected in parallel with each coil. This configuration creates an LC (inductor-capacitor) tank circuit. The tank circuit resonates at a specific frequency, f_o, which is determined as:

$$f_o = \frac{1}{2\pi\sqrt{\mathrm{LC}}} \tag{1}$$

where L represents the inductance of the coil, and C is the capacitance of the capacitor. The resonant frequency is a critical parameter because any conductive object in proximity to the coil mainly alters the inductance, consequently shifting the resonant frequency.

Here, for the detection of objects over a 2D domain which can be considered as an imaging process, we employ a 2D array of 4×4 planar coils with each coil having parameters shown in Table 1. By precisely measuring the changes in the resonant frequency of the tank circuits made with these coils, the system can effectively image conductive objects.

The data acquisition board in Fig. 2 consists of the LDC1614EVM module from Texas Instruments, a multiplexer board, and Arduino Mega 2560 as the microcontroller acting as an interface to acquire and send data to a PC. The LDC1614 is a high-resolution inductance-to-digital converter operation based on the measurement of a tank circuit with a resonant frequency below 10 MHz. Here, we have a 330 pF capacitor in parallel with each coil to make the tank circuit. Communication between LDC1614EVM and Arduino is handled via the I^2C protocol, using the default address 0x2A. The initial setup involves configuring the LDC1614 to read from one of the channels which acquires data from the array of sensors via multiplexing (to connect and measure one coil at a time to the LDC1614 channel). The system configuration includes setting the LDC1614's registers and initializing I^2C communication.

TABLE 1. Parameters of the inductive sensors.

Parameters	Value
Outer diameter	29 mm
Layers	2
Turns per layer	33
Trace width	0.152 mm
Spacing between traces	0.152 mm
Copper thickness	1oz-Cu
Spacing between 1^{st} and 2^{nd} layer	0.102 mm
Center-to-center distance between coils	35.4 mm
PCB substrate material	FR4

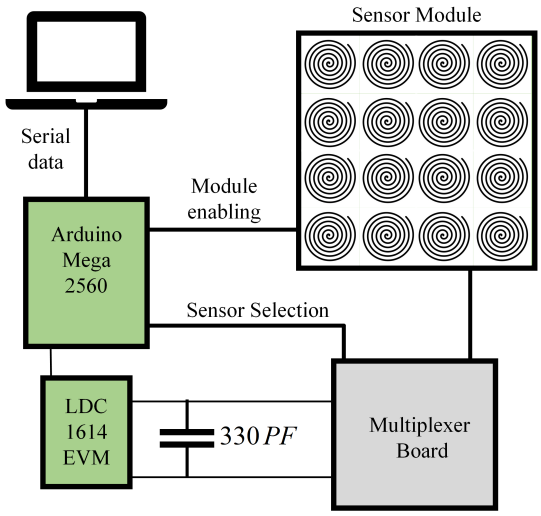

FIGURE 2. Schematic of the data acquisition system.

The LDC1614 parameters such as the reference count (RCOUNT0), settling count (SETTLECOUNT0), and clock dividers (CLOCK_DIVIDERS0) are critical for achieving desired resolution and sampling rates. A 330 pF capacitor is used for the tank circuit, affecting oscillation frequency and measurement sensitivity. Additionally, drive current and multiplexer settings are optimized, which is essential for handling multiple inductors effectively.

Data are acquired through reading specific LDC1614 registers by the Arduino microcontroller and are sent to a connected Python program on the PC via the serial interface. The program awaits a command from the Python side to initiate scanning and reading data sequentially from the selected inductor channel. Each measurement is followed by a reset to prepare the LDC1614 for the next operation. Various configurations allow for adjustments in drive current and other settings, accommodating different testing scenarios or inductor characteristics.

3. MULTI-LAYER PERCEPTRON

The multilayer perceptron (MLP) is a type of feedforward artificial neural network characterized by multiple fully connected layers. It employs backpropagation for optimizing the weights between nodes, enabling it to model complex nonlinear relationships. This versatility makes MLPs effective for various

tasks, including image and speech recognition, medical diagnosis, etc. [13].

Figure 3 illustrates the MLP architecture, consisting of an input layer, a hidden layer, and an output layer. Each neuron in one layer is connected to every neuron in the next, allowing the hidden layers to capture nonlinear relationships through activation functions, such as the Rectified Linear Unit (ReLU), which helps mitigate the vanishing gradient problem.

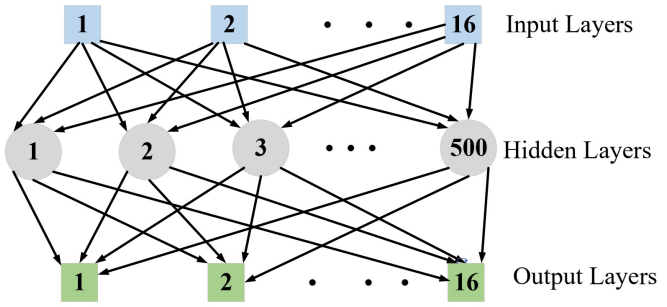

FIGURE 3. Layered diagram of MLP used in the proposed method.

Table 2 outlines the key parameters for the MLP classifier used in this work, featuring a hidden layer with 500 neurons, the Adam optimizer, an initial learning rate of 0.01, and a maximum of 1000 iterations.

TABLE 2. Key parameters of the used MLP classifier.

Parameters	Description
Hidden Layers	Single layer with 500 neurons
Solver	Adam
Activation	ReLU
Learning Rate Initialization	0.01
Maximum Iterations	1000

For these data, we conducted a comprehensive grid search over a range of hyperparameters, including different numbers of hidden layers, neurons, and learning rates, to identify the optimal configuration. Specifically, we explored models with 1 to 4 hidden layers, neurons ranging from 100 to 2000 per layer, and learning rates between 0.01 and 0.0001. Through this systematic search, we found that the optimal configuration for our dataset was a model with 1 hidden layer, 500 neurons, the Adam optimizer, and a learning rate of 0.01. This balance allowed us to achieve high accuracy on simpler tasks (single and double-object detection) while mitigating overfitting, particularly given the current limitations in the diversity of the training data.

4. IMAGING RESULTS

The setup of the novel AI-driven EII system is shown in Fig. 4. Central to this setup is the custom-designed sensors module, which comprises 16 inductors arranged in a 4×4 grid.

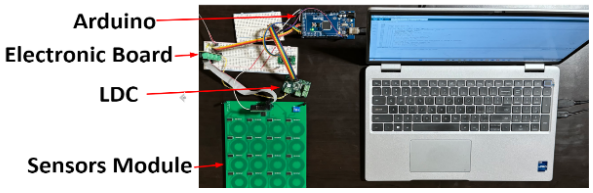

FIGURE 4. Picture of the imaging setup.

4.1. Data Acquisition

In the initial phase of data collection, measurements were taken with no metal objects placed under the module to establish baseline offsets for each sensor. Subsequently, square copper sheets with dimensions of 20 mm $\times$ 20 mm were positioned at a fixed distance of 15 mm beneath the sensor's module. This setup allowed for the precise measurement of electromagnetic responses. The collected data were then refined by subtracting the baseline offset and computing the percentage change for each sensor. Lastly, the percentage change data were mapped to a range of 0 to 1 (by adjusting them based on the minimum and maximum values of the responses of all sensors). This uniform scaling ensures that all features contribute equally, improving comparison and analysis, especially in the machine learning algorithm.

For scenarios involving a single object under the module, data were collected across 16 different cases, with each case being measured 30 times. This dataset was labeled as single object data (SOD). When two objects were placed under the sensor array, data were collected for 120 cases (various mutual positioning of the two objects) from each sensor, each measured 30 times and saved as double objects data (DOD). As the number of objects increased, the number of possible cases grew exponentially. For three objects under the sensor array, data were collected for 80 out of the possible 560 cases, each measured 30 times and saved as triple objects data (TOD).

4.2. Accuracy Definition

In the presented system for object recognition using the sensor module, each input dataset consists of 16 numbers from a set of 16 sensors. The output of the MLP-based algorithm yields 16 numbers, each indicating the probability of an object being detected by each of the 16 sensors (classes). If the probability of a data point being categorized in a class is higher than 80%, we set it to 1; otherwise, we set it to 0. Since the number of metal objects under the module can vary, it is essential to establish a specific definition of detection accuracy for different scenarios.

Consider a situation where X metal objects are placed under X sensors out of a total of 16 sensors, and there is no metal object under the other sensors. For different positions of the objects under the sensors, the responses are collected N times and given as input to the MLP system. In an ideal case, this system should recognize the correct locations of all X metal objects in all N data. However, there are situations where the system is not able to recognize all X objects and instead recognizes a smaller number of them. This is mainly due to the measurement of noises and parasitic effects. In this way, the

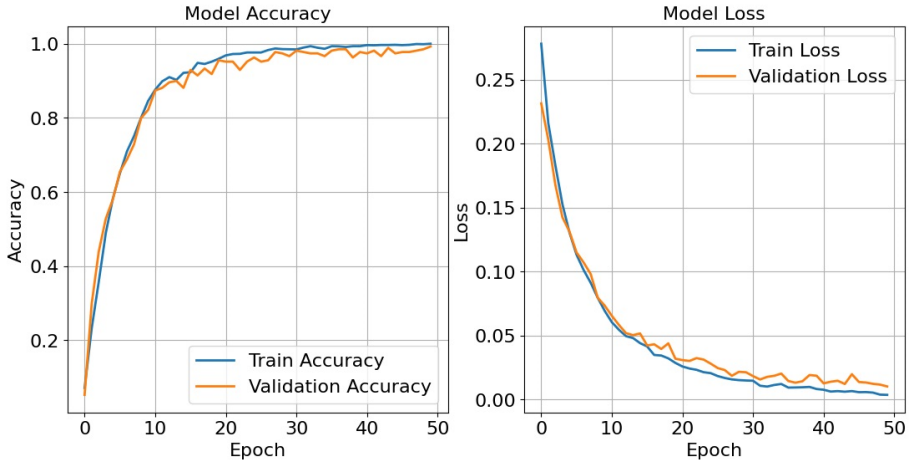

FIGURE 5. Performance metrics of the proposed MLP technique.

number of successful detections of K objects out of X objects is defined as P_K. Equation (2) clearly shows that the sum of success states is equal to the number of data taken:

$$\sum_{K=0}^{X} P_K = N \tag{2}$$

Then, the accuracy is defined as:

$$Accuracy = \frac{\sum_{K=0}^{X} KP_K}{NX} \times 100\% \tag{3}$$

4.3. Training Based on SOD

To evaluate the performance of the network, which is based on Multi-Layer Perceptron (MLP) architecture, we divided the dataset into three distinct parts: 60% for training, 20% for validation, and 20% for testing. This stratification ensures a robust assessment of the network's capabilities across different stages of learning.

The network was initially trained in the simplest form of data (SOD) to establish a baseline performance. Fig. 5 illustrates the network's efficacy over 50 epochs. The left figure presents the accuracy trajectories for the training, validation, and testing datasets individually.

These accuracy curves demonstrate that the network not only has been effectively trained but also generalizes well to unseen data. Notably, the model achieved a remarkable 97% accuracy on the test dataset related to SOD. This high level of accuracy indicates the network's strong ability to learn complex patterns and make accurate predictions.

The loss curves provide compelling evidence to reinforce these findings, illustrating a marked and sustained decrease in both training and validation loss over time. This consistent downward trend not only highlights the model's improved performance but also indicates its increasing ability to generalize effectively to unseen data. As the epochs progress, the convergence of the loss values suggests a robust learning process, further validating the effectiveness of the implemented training strategies.

Next, we evaluated the network's performance using test data associated with DOD and TOD. The aim is to enhance the network's ability to identify more complex objects, despite being trained on a limited dataset.

The network was applied to the collected DOD and TOD datasets, with accuracy calculated using the formula provided in (3) and summarized in Table 3.

TABLE 3. Test data accuracy based on proposed method.

Training Data	Accuracy		
	SOD	DOD	TOD
SOD	97%	79.9%	56.7%
SOD and half of DOD	97.3%	87.8%	78.1%

In calculating the accuracy for DOD, specific parameters were used: $X = 2$, $N = 3600$, The probabilities P_k were derived from the network based on its object detection accuracy, with $P_2 = 2593$, $P_1 = 568$, and $P_0 = 439$.

Substituting these values in (3) yielded an accuracy of 79.9%, which is considered acceptable for this stage. This result demonstrates the network's capability to effectively detect dynamic objects within the given constraints.

Figure 6(a) shows an example where the objects are positioned under inductors 3 and 10. The left image displays the raw data captured by the data acquisition system for the array of 4×4 sensors, showing a grid with various colored squares representing different values. The right image illustrates the output of the AI algorithm, highlighting the significant areas imaged by the system.

To assess the accuracy for TOD, certain parameters were applied: $X = 3$ and $N = 2400$. The probabilities P_k were obtained from the network according to its object detection performance, with values $P_3 = 567$, $P_2 = 781$, $P_1 = 823$, and $P_0 = 229$. By inserting these values in (3), an accuracy of 56.7% was achieved, which is deemed not satisfactory for this phase.

TABLE 4. Comparison of the accuracy of object detection method for two examples of Fig. 7.

Position of objects	Detected positions using different threshold levels			Detected positions by the proposed method
	Level = 0.6	**Level = 0.7**	**Level = 0.8**	
5, 7	4, 5, 7, 13, 16	4, 5, 7	7	5, 7
6, 13, 15	6, 7, 9, 12, 13, 15	6, 12, 13, 15	6, 13, 15	6, 13, 15

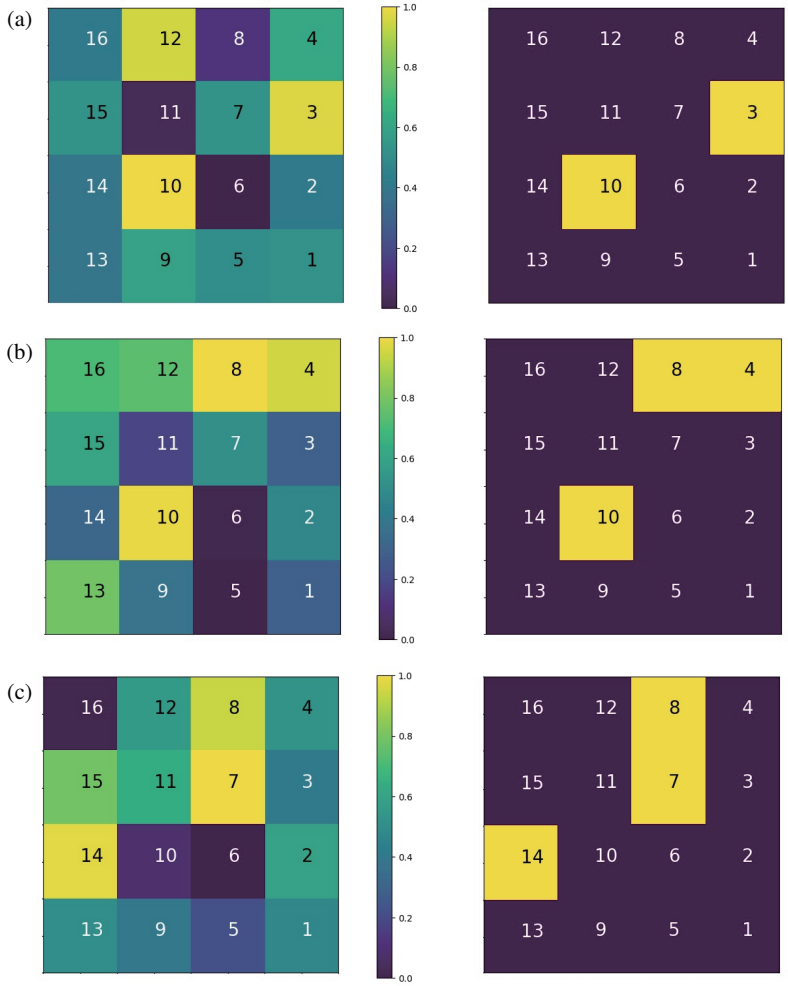

FIGURE 6. Results of implemented EII, (a) training based on SOD and testing with DOD, and (b) and (c) show two examples in which training is based on SOD and half of DOD and testing is done by TOD.

4.4. Training Based on SOD and Half of DOD

In this phase, we trained the network using 16 SOD measurements and 60 cases of DOD. As the number of training data increased, the accuracy for SOD did not change much and increased slightly to 97.3%. In calculating the accuracy for DOD, specific parameters were used: $X = 2$, $N = 1800$. The probabilities P_k were derived from the network based on its object detection accuracy, with $P_2 = 1434$, $P_1 = 291$, $P_0 = 75$. Using (3), the accuracy increased to 87.8%. Similarly, for TOD, specific parameters were used: $X = 3$, $N = 2400$, and the detection parameters were $P_3 = 874$, $P_2 = 1479$, $P_1 = 42$, and $P_0 = 5$, leading to an accuracy increase of 78.1% based on (3).

Figure 6(b) illustrates objects positioned beneath sensors 4, 8, and 10. The left image shows raw data from the acquisition system, with a grid of colored squares indicating different values. The right image presents the AI algorithm's output, highlighting the key areas identified. In Fig. 6(c), objects are under indicators 7, 8, and 14, with the left image, again, showing raw data and the right image displaying the AI's processed output with much better quality.

4.5. Comparing Proposed Method with a Thresholding Method

In this section, we compare the performance of the proposed AI-driven method with a conventional threshold-based ap-

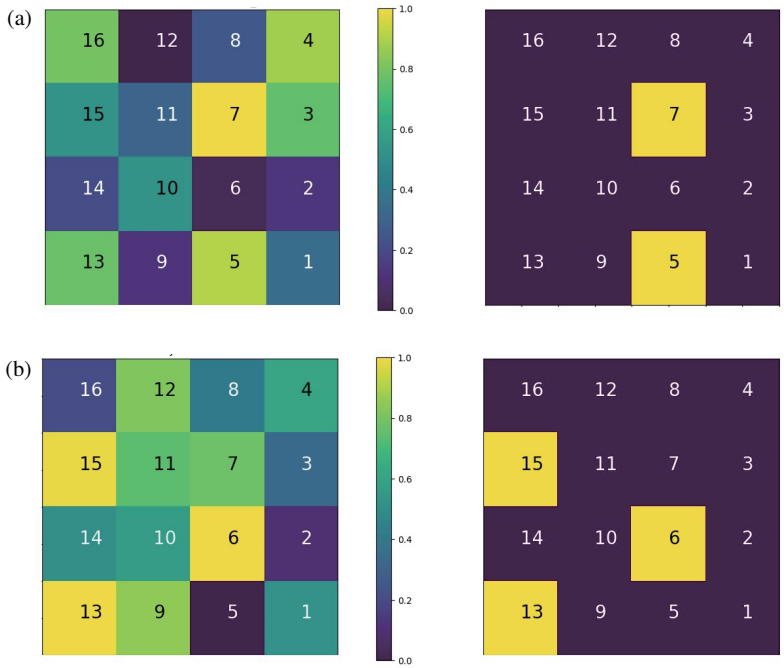

FIGURE 7. Results of implemented EII, (a) objects under 5 and 7 and (b) objects under 6, 13 and, 15.

proach for detecting metallic objects. Specifically, we examine the accuracy of object detection when applying fixed thresholds of 0.6, 0.7, and 0.8 on the raw sensors' data. Fig. 7 (parts a and b) showcases two examples, where the results of the detection using the proposed method are clearly highlighted. In these examples, the AI-based method successfully detects the exact locations of the metallic parts. On the other hand, as shown in Table 4, the threshold-based method fails to consistently identify the correct positions of the metallic objects. For instance, applying a threshold of 0.8 results in missed detections, while lower thresholds (0.6 and 0.7) lead to false positives, detecting metal objects in locations where they do not exist.

Table 5 further consolidates this comparison by presenting the overall detection accuracy across all test data using different thresholds. The results indicate that relying solely on a fixed threshold does not provide reliable detection, as the accuracy fluctuates significantly depending on the threshold value. In contrast, the proposed AI-based method demonstrates superior performance, achieving consistently high accuracy across both simple and complex detection scenarios. This comparison highlights the robustness and adaptability of the AI-driven approach, which is capable of learning intricate patterns and making accurate predictions without the need for manual threshold tuning. The significant improvement in detection accuracy, as shown in both Tables 4 and 5, underscores the effectiveness of the proposed method over traditional threshold-based techniques.

TABLE 5. Test data accuracy when using thresholding for detection.

Threshold Levels	Accuracy		
	SOD	DOD	TOD
0.6	66.4%	61.2%	52.1%
0.7	74.7%	63.1%	572%
0.8	68.1%	64.7%	53.7%

5. CONCLUSION AND DISCUSSION

This paper has introduced a novel proof-of-concept AI-driven approach to enhance the performance of EII systems, particularly in the context of detecting conductive objects over a 2D plane which can be considered as a 2D imaging process. Through the integration of an MLP classifier, our system has demonstrated robust learning capabilities and its potential for precise object detection. The experimental results underscore the efficacy of our approach. When trained with the SOD, the MLP achieved an impressive accuracy of over 97% for SOD and 79.9% for DOD. This highlights the system's significant improvements in both resolution and accuracy. Furthermore, when training with SOD and half of DOD and testing with DOD, the system maintained a high accuracy rate of 81.3% for DOD and 78.1% for TOD, demonstrating its ability to generalize effectively from limited training data and its competence in handling more complex imaging scenarios. These results affirm the potential of our AI-enhanced EII system to be employed in various real-time or quasi-real-time imaging applications, from security screening to industrial inspections.

Furthermore, to achieve higher resolution using the proposed technique, smaller sensors with more turns, more layers, or larger currents can be employed to improve the resolution while keeping the imaging distance (distance between the measurement aperture plane and object plane) sufficiently large. This allows the system to detect finer details in the imaged plane. Additionally, more advanced sensor multiplexing techniques

may be needed to efficiently manage the data from a larger array of sensors. Despite these potential upgrades, the overall imaging concept remains flexible and capable of handling both larger and higher-resolution imaging tasks with minimal modifications.

Lastly, we emphasize that with a large-scale system and proper training, the approach can be utilized for detection of multiple objects that can be physically connected over the 2D plane, forming a continuous large object. In that scenario, the outcome will be an image of that object. In other words, the goal of this project is to scale up the number of sensors in the system in the future. With a higher sensor density, the system will be capable of producing a more detailed representation of metallic objects, thus demonstrating true imaging capabilities, including the ability to capture geometric features.

ACKNOWLEDGEMENT

This work was supported in part by the U.S. National Science Foundation under Grant 1920098.

REFERENCES

[1] Ganesh, M., M. Ravan, and R. K. Amineh, "Electromagnetic induction imaging at multiple depths with a single coil," *IEEE Transactions on Instrumentation and Measurement*, Vol. 70, No. 4502809, 1–9, 2021.

[2] Peyton, A. J., Z. Z. Yu, G. Lyon, S. Al-Zeibak, J. Ferreira, J. Velez, F. Linhares, A. R. Borges, H. L. Xiong, N. H. Saunders, and M. S. Beck, "An overview of electromagnetic inductance tomography: Description of three different systems," *Measurement Science and Technology*, Vol. 7, No. 3, 261, 1996.

[3] Griffiths, H., "Magnetic induction tomography," *Measurement Science and Technology*, Vol. 12, No. 8, 1126, 2001.

[4] Ma, L., H.-Y. Wei, and M. Soleimani, "Planar magnetic induction tomography for 3D near subsurface imaging," *Progress In Electromagnetics Research*, Vol. 138, 65–82, 2013.

[5] Guilizzoni, R., J. C. Watson, P. Bartlett, and F. Renzoni, "Imaging by electromagnetic induction with resonant circuits," in *Image Sensing Technologies: Materials, Devices, Systems, and Applications II*, Vol. 9481, 135–146, 2015.

[6] Eichardt, R., C. H. Igney, J. Kahlert, M. Hamsch, M. Vauhkonen, and J. Haueisen, "Sensitivity comparisons of cylindrical and hemi-spherical coil setups for magnetic induction tomography," in *World Congress on Medical Physics and Biomedical Engineering*, 269–272, Munich, Germany, Sep. 2009.

[7] Zolgharni, M., H. Griffiths, and P. D. Ledger, "Frequency-difference MIT imaging of cerebral haemorrhage with a hemispherical coil array: Numerical modelling," *Physiological Measurement*, Vol. 31, No. 8, S111, 2010.

[8] Franceschini, S., M. Ambrosanio, F. Baselice, and V. Pascazio, "Neural networks for inverse problems: The microwave imaging case," in *2021 15th European Conference on Antennas and Propagation (EuCAP)*, 1–5, Dusseldorf, Germany, 2021.

[9] Ambrosanio, M., S. Franceschini, M. M. Autorino, and V. Pascazio, "Convolutional neural networks for tomographic MIMO ground penetrating radar imaging," in *2021 7th Asia-Pacific Conference on Synthetic Aperture Radar (APSAR)*, 1–5, Bali, Indonesia, Nov. 2021.

[10] Wei, Z. and X. Chen, "Deep-learning schemes for full-wave nonlinear inverse scattering problems," *IEEE Transactions on Geoscience and Remote Sensing*, Vol. 57, No. 4, 1849–1860, 2019.

[11] Li, L., L. G. Wang, F. L. Teixeira, C. Liu, A. Nehorai, and T. J. Cui, "DeepNIS: Deep neural network for nonlinear electromagnetic inverse scattering," *IEEE Transactions on Antennas and Propagation*, Vol. 67, No. 3, 1819–1825, 2019.

[12] Liu, R., Y. Li, F. Fu, F. You, X. Shi, and X. Dong, "Time-difference imaging of magnetic induction tomography in a three-layer brain physical phantom," *Measurement Science and Technology*, Vol. 25, No. 6, 065402, 2014.

[13] Al Bataineh, A., D. Kaur, and S. M. J. Jalali, "Multi-layer perceptron training optimization using nature inspired computing," *IEEE Access*, Vol. 10, 36 963–36 977, 2022.